Journal of Nuclear Medicine, published on August 30, 2018 as doi:10.2967/jnumed.118.214320

# Synthesis of patient-specific transmission data for PET attenuation correction for PET/MRI neuroimaging using a convolutional neural network

**Karl D Spuhler[1], John Gardus III[2], Yi Gao[3], Christine DeLorenzo[2], Ramin Parsey[2], Chuan Huang[1,2,4]**

[1] Biomedical Engineering, Stony Brook University

[2] Psychiatry, Stony Brook University Medical Center

[3]Health Science Center, Shenzhen University

[4]Radiology, Stony Brook University Medical Center.

First author: Karl D Spuhler. 700 Health Sciences Drive, Stony Brook, NY, 11790. Phone: 845-249-6836. Email: karl.spuhler@stonybrookmedicine.edu. (Graduate student).

Corresponding author: Chuan Huang. L4-120, Stony Brook University Medical Center, Stony Brook, NY 11794. Phone: 631-638-1536. Email: chuan.huang@stonybrookmedicine.edu

Word count: 4997

**Financial support:** This work is partially supported by NARSAD young investigator award (CH), Stony Brook Bridge Fund Program (CH). YG would like to thank support from National Natural Science Foundation of China No.61601302 and Shenzhen peacock plan (NO.KQTD2016053112051497).

**Running Title: CNNs for generating transmission data**

**ABSTRACT**

Attenuation correction is a notable challenge associated with simultaneous PET/MRI, particularly in neuroimaging, where sharp boundaries between air and bone volumes exist. This leads to concerns regarding the visual and, more specifically, quantitative accuracy of PET reconstructions for data obtained with PET/MRI. Recently developed techniques can synthesize attenuation maps using only MRI data and are likely adequate for clinical use, however, little work has been conducted to assess their suitability for the dynamic PET studies frequently employed in research to derive physiological information such as binding potential of neuroreceptors in a region. At the same time, existing PET/MRI attenuation correction methods are predicated upon synthesizing CT data, which is not ideal, as CT data are acquired with much lower energy photons than PET data and thus do not optimally reflect the PET attenuation map. **Methods:** We trained a convolutional neural network to generate patient-specific transmission data from T1-weighted MRI. Using the trained network, we generated transmission data for a testing set comprising 11 subjects scanned with 11C-WAY-100635 and 10 subjects scanned with 11C-DASB. We assessed both static and dynamic reconstructions. For dynamic PET data, we report differences in $BP_{ND}$ and $BP_F$ for 11C-WAY-100635 and $V_T$ for 11C-DASB. **Results:** The mean bias for generated transmission data was -1.06±0.81%. Global biases in static PET uptake were -0.49±1.7%, and -1.52±0.73% for 11C-WAY-100635 and 11C-DASB, respectively. **Conclusions:** Our neural network approach is capable of synthesizing patient-specific transmission data with sufficient accuracy for both static and dynamic PET studies.

## INTRODUCTION

The benefits of PET/MRI are perhaps nowhere more impactful than they are to neuroimaging, with PET/MRI standing to significantly improve the quality of quantitative neuroimaging-driven studies in the psychiatric community (*1*), offering several benefits such as reduced radiation burden, motion-correction (*2*), partial volume correction (*3*) and MRI-guided PET reconstruction (*4,5*). Despite these promised benefits, PET/MRI attenuation correction remains a nontrivial problem, particularly in the head and neck where sharp boundaries between air and bone exist in the FOV.

Historically, PET attenuation correction has been straightforward: standalone scanners utilize a rotating nuclear transmission source (TX-AC; transmission attenuation correction), deriving the attenuation map with the same 511keV photons imaged in PET, while PET/CT scanners make use of the photon attenuation data provided by CT (CT-AC; CT attenuation correction). In PET/MRI, the strong magnetic field and limited space within the magnet obviate the possibility of implementing either technique (*6,7*).

CT-AC and TX-AC techniques exhibit contrasting benefits and drawbacks. TX-AC theoretically provides a direct representation of the patient's attenuation map, given the fact that 511keV photons are used to acquire the attenuation data. On the other hand, CT-AC must account for several nonidealities, most notably the fact that attenuation values determined using CT must be adjusted in order to account for the four-to-five factor difference in CT and PET photon energies. This has been shown to lead to significant and heterogeneous overestimation of attenuation coefficients and radiotracer uptake (*8,9*). This is exacerbated by the polychromatic nature of CT beams (*10*), which obfuscates the effective energy at which attenuation coefficients are determined and subjects CT-AC maps to beam hardening artifacts. From a research perspective, it is equally concerning that multiple methods exist for correcting these problems; CT-AC techniques can differ in terms of both the CT acquisition used, as well as the processing steps used in order to perform energy scaling (*9*). Given its ease of acquisition, CT-AC has

become the preeminent technique for clinical scanning. Despite this, CT cannot be considered a genuine gold standard for attenuation correction data (*11*), and a recent multi-center review of several clinically acceptable PET/MRI attenuation protocols stated that not comparing to gold standard transmission scans was a limitation (*12*).

Techniques for deriving attenuation maps in PET/MRI generally fall into two categories: those which employ specialized pulse sequences such as ultrashort or zero TE (UTE, ZTE, respectively) (*13-16*) and those which seek to generate pseudo-CT data from an atlas of matched MRI and CT data (*12,17,18*). These techniques demonstrate unique shortcomings, outside of their reliance upon CT gold standard for evaluation or function. In particular, MRI-alone methods consume scan time which could be dedicated to other sequences, and typically assign predetermined attenuation values to any number of segmented tissue classes (*19*); this prevents MRI-alone methods from accurately reflecting differences in bone density. At the same time, while atlas-based methods seek to reflect patient-specific attenuation values, they are dependent upon accurate registration of the atlas onto the input MRI volume. While certain techniques, such as patch-based learning, have been presented to mitigate the effects of misregistration (*17,20*), no truly registration-free atlas-based method has been independently evaluated in the literature.

Alongside these limitations is the concern that little task-based validation of published methods' suitability for kinetic modelling has been conducted (*21*). Given the proportion of PET/MRI scanning dedicated to research (*22*), this represents a gap in the literature. There is reasonable concern regarding the parameters obtained in dynamic PET studies; a side-by-side comparison of several PET/MRI attenuation correction techniques in 18F-FDG, 11C-PiB and 18F-florbetapir demonstrated tracer-dependent differences in performance across all methods (*12*). This dependence upon tracer distribution is a possible source of error in dynamic PET/MRI studies given the varying dynamics of the radiotracer throughout the brain during the scan. Encouragingly, recent work has demonstrated the stability of a pseudo-CT technique for kinetic

modelling of 18F-MPPF (*21*), although this study was limited and examined kinetic modelling of only a single radiotracer.

The emergence of convolutional neural networks (CNN) has led to considerable examination of their feasibility of synthesizing patient specific attenuation correction data for PET/MRI. Whereas initial works focused only on the quantitative accuracy of CNN-derived pseudo-CT images (*23*), recent studies have demonstrated accurate PET reconstruction. A CNN model depending on T1-weighted MRI data was shown to yield accurate PET reconstructions, although reconstruction analysis was confined to a small cohort and only analyzed short acquisitions of a single radiotracer (*24*). More recently, models depending upon Dixon or a combination of Dixon and ZTE were seen to provide accurate static PET reconstructions, although these models depend upon additional MRI sequences and were again only validated in a single radiotracer (*25*); a similar approach based on Dixon and ZTE data was shown to yield significantly more accurate PET quantitation than vendor-implemented PET/MRI attenuation correction techniques in scans of the pelvis (*26*). Whereas CNN-based PET/MRI attenuation map generation is an established technique, there are unaddressed limitations in the field: no technique has been compared to gold standard transmission data, all analyses have been confined to a single radiotracer and—most importantly for neuroimaging research communities—no technique has been validated for kinetic modelling of PET data.

Here, we demonstrate the suitability of generating pseudo-TX data with a CNN using only T1-weighted MRI. We demonstrate that this method is well-suited for static and dynamic PET analysis using data previously collected using multiple radiotracers: 11C-WAY-100635, an agonist of the serotonin-binding 5-$HT_{1A}$ receptor (*27*) and 11C-DASB, which targets the serotonin transporter (5-HTT) (*28*).

## MATERIALS AND METHODS

### Subject population

The institutional review board approved this retrospective study and the requirement to obtain informed consent was waived.

We queried all de-identified scans in our database who had previously been scanned using both standalone PET and MRI. PET transmission data were extracted alongside the PET emission and MRI data.

The largest single radiotracer dataset available consisted of 66 individuals scanned using 11C-WAY-100635. These individuals were randomly partitioned into training (N=44), validation (N=11) and testing (N=11) datasets.

Following validation of our method with 11C-WAY-100635 we similarly assessed performance for 10 subjects scanned with 11C-DASB.

**MRI Acquisition**

MRI acquisition consisted of identical pulse sequences on the same scanner for subjects in both the 11C-WAY-100635 and 11C-DASB datasets. All MRI was performed on a GE 1.5T Signa Advantage. MRI was acquired using a spoiled gradient recalled acquisition (SPGR). Pulse sequence parameters were as follows: TE=2.8ms; TR=7.0ms; TI=500ms; acquisition matrix: 256x256x170; coronal slices; voxel size: 1.0mm isotropic. SPGR was the only CNN input utilized.

**PET Acquisition, Reconstruction and Modeling**

PET data for both radiotracers were acquired on a Siemens ECAT HR+. 68Ge transmission data were acquired for 10 minutes prior to the injection of a single intravenous bolus of up to 185MBq. Arterial input functions were obtained during the acquisitions. Arterial blood was drawn periodically throughout scans with both radiotracers, metabolite correction was performed using previously described methods for both 11C-WAY-100635 (*29*) and 11C-DASB (*30*). Static and dynamic reconstructions were performed with synthesized and ground truth transmission data using filtered back projection. Dynamic PET data were motion-corrected by rigidly registering each frame onto a reference frame as previously described (*31*). Static images were formed by averaging the final ten motion-corrected frames. PET reconstructions were registered onto their

accompanying T1-weighted MRI for region of interest (ROI) analysis using FLIRT (*32*). ROIs were determined using a previously described, automated technique (*33*).

Kinetic modelling was used in order to derived physiological parameters from dynamic PET data. For 11C-WAY-100635 we derive two binding potential parameters, $BP_F$ and $BP_{ND}$, which are commonly reported estimates of neuroreceptor density. For 11C-DASB we report the volume of distribution, $V_T$, the ratio of concentration in tissue relative to plasma. Kinetic modelling techniques for each tracer are provided in the sections detailing their specific acquisition.

**11C-WAY-100635 Acquisition and Modeling**

Emission data were collected for 110 minutes and binned into 20 frames (Frame duration: 3×20s, 3×1min, 3×2min, 2×5min, 9×10min). $BP_F$ and $BP_{ND}$ were derived using a constrained two tissue compartmental model, with cerebellar white matter used as reference tissue as previously described (*34,35*).

$BP_F$ and $BP_{ND}$ are defined thusly:

$$BP_F = \frac{V_T - V_{ND}}{f_p}$$

$$BP_{ND} = \frac{V_T - V_{ND}}{V_{ND}}$$

Where $V_T$ is the volume of distribution in the region of interest, $V_{ND}$ the volume of distribution in the reference region, and $f_p$ is the amount of radiotracer freely available in the plasma.

**11C-DASB Acquisition and Modeling**

Emission data were collected for 120 minutes and binned into 21 frames (Frame duration: 3x20s, 3x1min, 3x2mins, 2x5mins, and 10x10mins). Outcome measures were derived using likelihood estimation in graphical analysis (LEGA) (*36*), which has been reported to be the most stable method of modelling 11C-DASB (*37*). Given that no brain region is devoid of

specific 11C-DASB binding (*28,30*), we report $V_T$, which has been shown to be the only reproducible 11C-DASB modelling measure in test-retest studies (*37*).

**Preprocessing**

MRI images were first downsampled to 2mm isotropic resolution and normalized using Freesurfer (*38*). For the transmission images of the training and validation sets, areas outside of the brain, notably the scanner bed, were cropped out of the transmission data as the network would have no ability to synthesize them from the MRI images. Following this, atlas transmission images were rigidly registered to their matched MRI volume using FLIRT.

**CNN Design**

Patient-specific pseudo-TX data were generated using a CNN implemented in Tensorflow (*39*). The network made use of a uNet architecture (*40*), as shown in Figure 1. Upsampling was performed using transposed convolutions. The network was implemented for 2-dimensional inputs and synthesizes whole-volume data slice-by-slice. Five consecutive axial slices, centered on the slice to be synthesized, are presented to the network as unique channels. All activation functions were chosen to be rectified linear units (ReLU).

**CNN Training**

The CNN was trained using two Nvidia Tesla K80 GPUs on a workstation running Ubuntu 14.04. Pairs of MRI and transmission volumes were presented to the network axially on a slice-by-slice basis. The training objective was the minimization of L1-error between synthesized and ground truth transmission slices. In addition, L2-regularization was incorporated into the cost function in order to improve generalizability to the external testing sets. The Adam optimizer was used for updating during backpropagation (*41*). Data were presented to the network one subject at a time, without employing batches.

The validation set was passed through the network following each epoch. Training was halted whenever the total cost across the validation set increased for 5 consecutive epochs. The model converged after 32 hours of training. Once trained, whole volume TX data can be synthesized in about 1 second.

**CNN Evaluation**

Following training, we examined the similarity of synthesized transmission data to ground truth, as well as the quantitative accuracy of PET reconstructions making use of the synthesized transmission data.

**Synthesized Transmission Data**

Previously masked scanner beds were added to the synthesized data prior to PET reconstruction. Synthesized attenuation maps were compared to scanner transmission data on the basis of mean bias:

$$Bias = Mean\left(\frac{\mu_{synth} - \mu_{raw}}{\mu_{raw}}\right) * 100\%$$

Where $\mu_{synth}$ represents the attenuation coefficients in voxels of the CNN-derived transmission data, and $\mu_{raw}$ indicates those of the ground truth transmission data. Areas outside of the head, which are identical for synthesized and ground truth data, were not included.

**Static PET Analysis**

Masks were generated by taking the intersection of FSL-derived brain masks (*42*) and voxels with at least 20% of maximum PET activity in the ground truth reconstruction. This was done for consistency with a recent side-by-side comparison of many proposed PET/MRI attenuation correction techniques (*12*). For voxels contained within this mask, mean biases are reported along with standard deviation. We present these data at both the global and ROI-level. All ROIs were tested for statistically significant errors using Student's t-test.

### Kinetic Modelling Analysis

$V_T$, $BP_F$ and $BP_{ND}$ were estimated as described above. We report the mean bias and standard deviation in each ROI. Student's t-test was again used to determine whether ROIs exhibited statistically significant errors.

## RESULTS

### Synthesized Transmission Data

Synthesized attenuation maps demonstrated a slight negative bias, the mean relative bias between the synthesized and ground truth maps was seen to be -1.06±0.81%.

Figure 2 shows a representative pseudo-TX map alongside its accompanying ground truth data. Slices in the sinus region were chosen due to their complexity relative to superior slices.

### Static PET Analysis

Relative to ground truth, 11C-WAY-100635 PET images reconstructed using synthesized attenuation data demonstrated a mean relative bias -0.49%±1.7%. 11C-DASB images demonstrated a mean relative bias of -1.52±0.73%. Figure 3 shows slices of ground truth and reconstructed PET images alongside percent error maps for each radiotracer.

Static PET analysis was continued by examining relative biases at the ROI-level. Figure 4 illustrates subject-specific ROI biases. Student's t-test did not suggest statistically significant errors in any ROIs for either radiotracer.

### Dynamic PET Analysis

Kinetic modeling results for all radiotracers are shown in Figure 5. For 11C-WAY-100635, between $BP_F$ and $BP_{ND}$, $BP_F$ was generally more stable, with mean biases closer to zero as well as lower standard deviations of the error in the majority of ROIs. Using Student's t-test, no statistically significant errors were in either radiotracer.

## DISCUSSION

The presented method improves upon the state-of-the-art in two important ways. Our primary contribution is the validation of a PET/MRI attenuation correction method predicated upon gold standard nuclear transmission data, which provides more accurate quantitation than CT data. Secondly, we have approached this issue using a CNN; this allows us to circumvent the atlas registration requirements of many current pseudo-CT protocols. An interesting consideration motivated by this would be the technique's performance on subjects with non-standard anatomies relative to currently published pseudo-CT techniques, although no subjects with remarkable anatomical deviation were available for analysis. Future work investigating the utility of CNN-derived attenuation maps would certainly benefit from evaluation against more traditional techniques in the presence of anatomical deviations.

The primary motivation of this work is that TX data provides a more accurate representation of the subject's attenuation map than CT data given the large energy difference between PET and CT photons. In addition to this, TX data can be argued to have additional benefits given that the attenuation data are collected using the same detector system as the PET emission data. Unfortunately, in the present state, an analysis of these effects is not possible given that only retrospective TX data are available. This relates to the primary limitation of the proposed method, namely that a proper validation of the method using MRI and PET emission data collected on a simultaneous PET/MRI scanner, alongside subject-specific TX data, cannot be provided. Pseudo-TX attenuation maps applied to PET/MRI data yielded noticeably greater PET values throughout the brain—most notably the cortical areas—in comparison to standard vendor methods, although direct comparison is not possible due to the lack of gold standard attenuation data. An example 18F-FDG reconstruction is provided as Supplemental data.

Prospective study is warranted in light of the lack of direct validation on a PET/MRI scanner. This will require the assembly of a PET/MRI T1-weighted MRI and TX database for several subjects. Collecting such a database will require scans specific to this task, however,

multiple solutions exist. Primarily, institutions equipped with a standalone PET scanner can seek volunteers willing to receive a brief T1-weighted study on a simultaneous PET/MRI. At the same time, the feasibility of a fixed torus geometry for TX scanning on the Siemens Biograph mMR has been demonstrated (*43*). Although a modern database suitable to PET/MRI data is certainly required going forward, this necessity is addressable.

Our method is not based on any assumptions about anatomy, or the nature of the transformation between MRI and transmission data. As such, it is flexible, and could be easily adapted to accept additional MRI sequences, such as UTE or ZTE, into the training process. Any MRI contrast which can be reliably resampled to the same space as the input T1-weighted data could be simply as an additional input channel. As data were collected from a retrospective study which only employed MRI to delineate PET regions of interest, this was not possible in the current analysis.

The presented work, a validation of multiple dynamic PET measures in multiple radiotracers, adds to the existing literature in several important ways. To the best of our knowledge, only one study to date has examined the suitability of synthesized attenuation correction data (pseudo-CT) for dynamic PET studies (*21*). The previous work employed 18F-MPPF, a 5-$HT_{1A}$ binding tracer, for kinetic analysis. Our work adds additional evidence to their conclusion that synthesized attenuation data is sufficient for kinetic modeling of PET data. By employing multiple radiotracers probing different aspects of neurobiology, we have added significant generalizability to the prior work's observations. This is crucial, as PET/MRI attenuation correction methods have been shown to exhibit varying performance with different radiotracers in static analysis (*12*). At the same time, our work generates data with comparable accuracy but relative to a higher gold standard in the fact that the 18F-MPPF analysis used CT-AC.

The cerebellum is an extremely important region in dynamic PET neuroimaging, as the cerebellum white matter expresses many neuroreceptors of interest in far lower concentrations than cerebral regions. As such, it is a frequently employed area for the kinetic modelling of a large

number of radiotracers, including those used in this work. Given the reasonably accurate assumption of no specific binding occurring in the reference region, one can easily estimate the nondisplaceable volume of distribution ($V_{ND}$), thus providing an estimation of the amount of signal measured in other ROIs which is not related to the tracer binding to its targeted neuroreceptor. In this work, we observe highly accurate cerebellar uptake estimations using our synthesized transmission data. This is crucial to the accuracy of such kinetic studies and our demonstrated accuracy in $BP_F$ and, in particular, $BP_{ND}$ modelling would not have been possible without accurate measurements of cerebellar activity. Relatively few studies have placed an emphasis on the effects of various attenuation correction paradigms on cerebellar activity, which severely limits the confidence with which they can be applied to dynamic PET studies.

Despite the use of a separate tracer and parcellation strategies, we report $BP_{ND}$ biases with similar magnitude to those previously described. Further, our results add to those of the previous 18F-MPPF study by demonstrating the suitability of our technique for $BP_F$ estimation, which is the PET parameter most closely related to receptor density. Despite the ideality of estimating $BP_F$, it is dependent upon repeated, invasive blood sampling and subsequent metabolite analysis; because of this, $BP_{ND}$ is a more reported metric.

Generally speaking, $BP_F$ estimations were found to be more stable than $BP_{ND}$ in the 11C-WAY-100635 testing dataset. This was largely expected given the formulae used to derive each expression. $BP_F$ estimations are normalized to the amount of free radiotracer in the plasma, while $BP_{ND}$ estimations are normalized to the volume of distribution in some reference region, in this case the white matter of the cerebellum. As such, errors in reference region modeling compound errors in $BP_{ND}$ quantitation more than they do for $BP_F$.

To contextualize our reported biases in PET quantitation, 11C-WAY-100635 $BP_F$ quantitation is associated with an average test-rest variability of 9% (*33*). No ROI's ±1SD range intersects this inherent uncertainty. Moreover, $V_T$ estimation in [11]-DASB data has been shown

to exhibit an inherent test-retest variability of 5.5% (*37*). Static reconstruction biases are well within the test-retest reproducibility of PET imaging in both cases.

## CONCLUSION

Synthesizing pseudo-TX data using CNNs is a promising technique for attenuation correction in psychiatric PET/MRI. CNN-based attenuation demonstrates comparable accuracy to currently optimally performing techniques, while possibly obviating some nonidealities exhibited by current techniques such as the necessity for registration of prospective data onto a predefined atlas. Moreover, the technique presented here is suitable for static and dynamic PET imaging.

## ACKNOWLEDGEMENTS

This work is partially supported by NARSAD young investigator award (CH), Stony Brook Bridge Fund Program (CH). YG would like to thank the support from National Natural Science Foundation of China No.61601302 and Shenzhen peacock plan (NO.KQTD2016053112051497).

## REFERENCES


**1.** Catana C, Drzezga A, Heiss W-D, Rosen BR. PET/MRI for neurologic applications. *J Nucl Med.* 2012;53:1916-1925.

**2.** Huang C, Ackerman JL, Petibon Y, et al. Motion compensation for brain PET imaging using wireless MR active markers in simultaneous PET–MR: Phantom and non-human primate studies. *NeuroImage.* 2014;91:129-137.

**3.** Grecchi E, Veronese M, Bodini B, et al. Multimodal partial volume correction: Application to [11C] PIB PET/MRI myelin imaging in multiple sclerosis. *J Cereb Blood Flow Metab.* 2017:0271678X17712183.

**4.** Zaidi H, Becker M. The Promise of Hybrid PET/MRI: Technical advances and clinical applications. *IEEE Signal Process Mag.* 2016;33:67-85.

**5.** Ehrhardt MJ, Markiewicz P, Liljeroth M, et al. PET reconstruction with an anatomical MRI prior using parallel level sets. *IEEE Trans Med Imaging.* 2016;35:2189-2199.

**6.** Delso G, Fürst S, Jakoby B, et al. Performance measurements of the Siemens mMR integrated whole-body PET/MR scanner. *J Nucl Med.* 2011;52:1914-1922.

**7.** Wagenknecht G, Kaiser H-J, Mottaghy FM, Herzog H. MRI for attenuation correction in PET: methods and challenges. *MAGMA.* 2013;26:99-113.

**8.** Nakamoto Y, Osman M, Cohade C, et al. PET/CT: comparison of quantitative tracer uptake between germanium and CT transmission attenuation-corrected images. *J Nucl Med.* 2002;43:1137-1143.

**9.** Teimourian B, Ay MR, Zafarghandi MS, Ghafarian P, Ghadiri H, Zaidi H. A novel energy mapping approach for CT-based attenuation correction in PET. *Med phys.* 2012;39:2078-2089.

**10.** Kachelrieb M, Kalender WA. Improving PET/CT attenuation correction with iterative CT beam hardening correction. *IEEE Nucl Sci Symp Conf Rec* , 2005.

**11.** Malone IB, Ansorge RE, Williams GB, Nestor PJ, Carpenter TA, Fryer TD. Attenuation correction methods suitable for brain imaging with a PET/MRI scanner: a comparison of tissue atlas and template attenuation map approaches. *J Nucl Med.* 2011;52:1142-1149.

**12.** Ladefoged CN, Law I, Anazodo U, et al. A multi-centre evaluation of eleven clinically feasible brain PET/MRI attenuation correction techniques using a large cohort of patients. *NeuroImage.* 2017;147:346-359.

**13.** Catana C, van der Kouwe A, Benner T, et al. Toward implementing an MRI-based PET attenuation-correction method for neurologic studies on the MR-PET brain prototype. *J Nucl Med.* 2010;51:1431-1438.

**14.** Du J, Carl M, Bydder M, Takahashi A, Chung CB, Bydder GM. Qualitative and quantitative ultrashort echo time (UTE) imaging of cortical bone. *J Magn Reson.* 2010;207:304-311.

**15.** Yang J, Wiesinger F, Kaushik S, et al. Evaluation of Sinus/Edge-Corrected Zero-Echo-Time-Based Attenuation Correction in Brain PET/MRI. *J Nucl Med: official publication, Society of Nuclear Medicine.* 2017;58:1873-1879.

**16.** Sekine T, Ter EV, Warnock G, et al. Clinical evaluation of zero-echo-time attenuation correction for brain 18F-FDG PET/MRI: comparison with atlas attenuation correction. *J Nucl Med: official publication, Society of Nuclear Medicine.* 2016;57:1927-1932.

**17.** Torrado-Carvajal A, Herraiz JL, Alcain E, et al. Fast patch-based pseudo-CT synthesis from T1-weighted MR images for PET/MR attenuation correction in brain studies. *J Nucl Med.* 2016;57:136-143.

**18.** Izquierdo-Garcia D, Hansen AE, Förster S, et al. An SPM8-based approach for attenuation correction combining segmentation and nonrigid template formation: application to simultaneous PET/MR brain imaging. *J Nucl Med.* 2014;55:1825-1830.

**19.** Huang C, Ouyang J, Reese T, Wu Y, El Fakhri G, Ackerman J. Accurate measurement of bone attenuation in PET-MR. *J Nucl Med.* 2015;56:258-258.

**20.** Spuhler K, Huang C, DeLorenzo C, Parsey R. Patient-specific transmission volume synthesis for attenuation correction in simultaneous PET/MR. *J Nucl Med.* 2017;58:646-646.

**21.** Mérida I, Reilhac A, Redouté J, Heckemann RA, Costes N, Hammers A. Multi-atlas attenuation correction supports full quantification of static and dynamic brain PET data in PET-MR. *Phys Med Biol.* 2017;62:2834.

**22.** Fendler WP, Czernin J, Herrmann K, Beyer T. Variations in PET/MRI operations: Results from an international survey among 39 active sites. *J Nucl Med.* 2016;57;2016-2021.

**23.** Han X. MR-based synthetic CT generation using a deep convolutional neural network method. *Med phys.* 2017;44:1408-1419.

**24.** Liu F, Jang H, Kijowski R, Bradshaw T, McMillan AB. Deep learning MR imaging–based attenuation correction for PET/MR imaging. *Radiology.* 2017;286:676-684.

**25.** Gong K, Yang J, Kim K, El Fakhri G, Seo Y, Li Q. Attenuation Correction for Brain PET imaging using Deep Neural Network based on Dixon and ZTE MR images. *Phys Med Biol.* 2018.

**26.** Leynes AP, Yang J, Wiesinger F, et al. Zero-Echo-Time and Dixon Deep Pseudo-CT (ZeDD CT): Direct Generation of Pseudo-CT Images for Pelvic PET/MRI Attenuation Correction Using Deep Convolutional Neural Networks with Multiparametric MRI. *J Nucl Med.* 2018;59:852-858.

**27.** Pike VW, McCarron JA, Lammertsma AA, et al. Exquisite delineation of 5-HT1A receptors in human brain with PET and [carbonyl-11C] WAY-100635. *Eur J Pharmacol.* 1996;301:R5-R7.

**28.** Nørgaard M, Ganz M, Svarer C, et al. Cerebral serotonin transporter measurements with [11C] DASB: A review on acquisition and preprocessing across 21 PET centres. *J Cereb Blood Flow Metab.* 2018 (*In press*).

**29.** Martinez D, Hwang D-R, Mawlawi O, et al. Differential occupancy of somatodendritic and postsynaptic 5HT1A receptors by pindolol: a dose-occupancy study with [11C] WAY 100635 and positron emission tomography in humans. *Neuropsychopharmacology.* 2001;24:209-229.

**30.** Parsey RV, Kent JM, Oquendo MA, et al. Acute occupancy of brain serotonin transporter by sertraline as measured by [11C] DASB and positron emission tomography. *Biol Psychiatry.* 2006;59:821-828.

**31.** Kaufman J, Sullivan GM, Yang J, et al. Quantification of the serotonin 1A receptor using PET: Identification of a potential biomarker of major depression in males. *Neuropsychopharmacology.* 2015;40:1692-1699.

**32.** Jenkinson M, Smith S. A global optimisation method for robust affine registration of brain images. *MedI image anal.* 2001;5:143-156.

**33.** Parsey RV, Slifstein M, Hwang D-R, et al. Validation and reproducibility of measurement of 5-HT1A receptor parameters with [carbonyl-11C] WAY-100635 in humans: comparison of arterial and reference tissue input functions. *J Cereb Blood Flow Metab.* 2000;20:1111-1133.

**34.** Milak MS, DeLorenzo C, Zanderigo F, et al. In vivo quantification of human serotonin 1A receptor using 11C-CUMI-101, an agonist PET radiotracer. *J Nucl Med.* 2010;51:1892-1900.

**35.** Lan MJ, Hesselgrave N, Ciarleglio A, et al. Higher pretreatment 5-HT1A receptor binding potential in bipolar disorder depression is associated with treatment remission: A naturalistic treatment pilot PET study. *Synapse.* 2013;67:773-778.

**36.** Ogden RT. Estimation of kinetic parameters in graphical analysis of PET imaging data. *Stat med.* 2003;22:3557-3568.

**37.** Ogden RT, Ojha A, Erlandsson K, Oquendo MA, Mann JJ, Parsey RV. In vivo quantification of serotonin transporters using [11C] DASB and positron emission tomography in humans: modeling considerations. *J Cereb Blood Flow Metab.* 2007;27:205-217.

**38.** Sled JG, Zijdenbos AP, Evans AC. A nonparametric method for automatic correction of intensity nonuniformity in MRI data. *IEEE Trans Med Imaging.* 1998;17:87-97.

**39.** Abadi M, Agarwal A, Barham P, et al. Tensorflow: Large-scale machine learning on heterogeneous distributed systems. *arXiv preprint arXiv:160304467.* 2016.

**40.** Ronneberger O, Fischer P, Brox T. U-net: Convolutional networks for biomedical image segmentation. *International Conference on Medical Image Computing and Computer-Assisted Intervention,* 2015.

**41.** Kingma D, Ba J. Adam: A method for stochastic optimization. *arXiv preprint arXiv:14126980.* 2014.

**42.** Smith SM. Fast robust automated brain extraction. *Hum brain mapp.* 2002;17:143-155.

**43.** Bowen SL, Fuin N, Levine MA, Catana C. Transmission imaging for integrated PET-MR systems. *Phys Med Biol.* 2016;61:5547.

## FIGURES

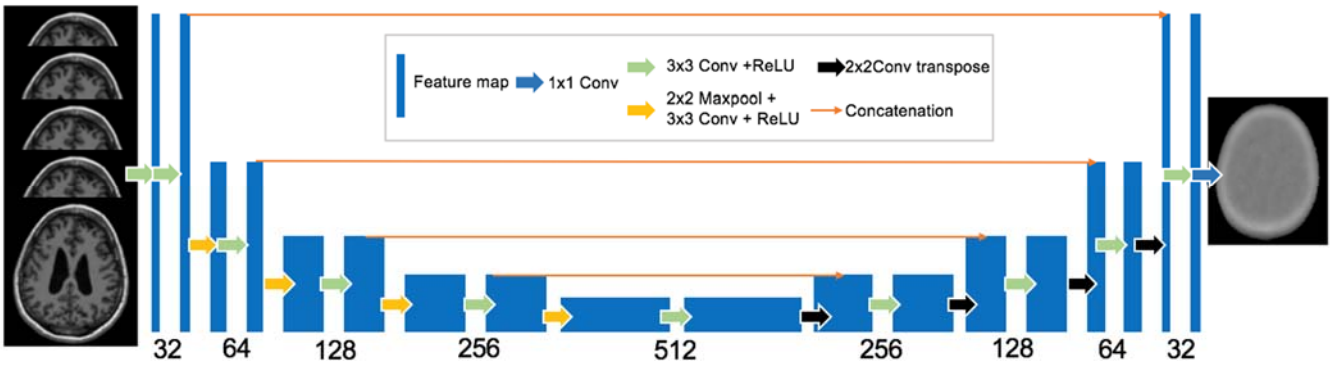


*FIGURE 1. CNN architecture. Numbers indicate the number of features at each layer.*

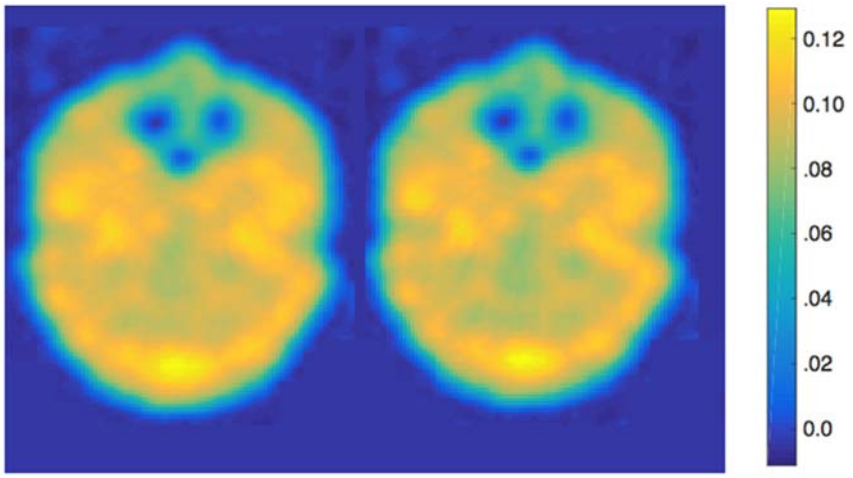


FIGURE 2. Side-by-side comparison of synthesized (left) and ground truth (right) TX-AC data for a randomly selected subject.

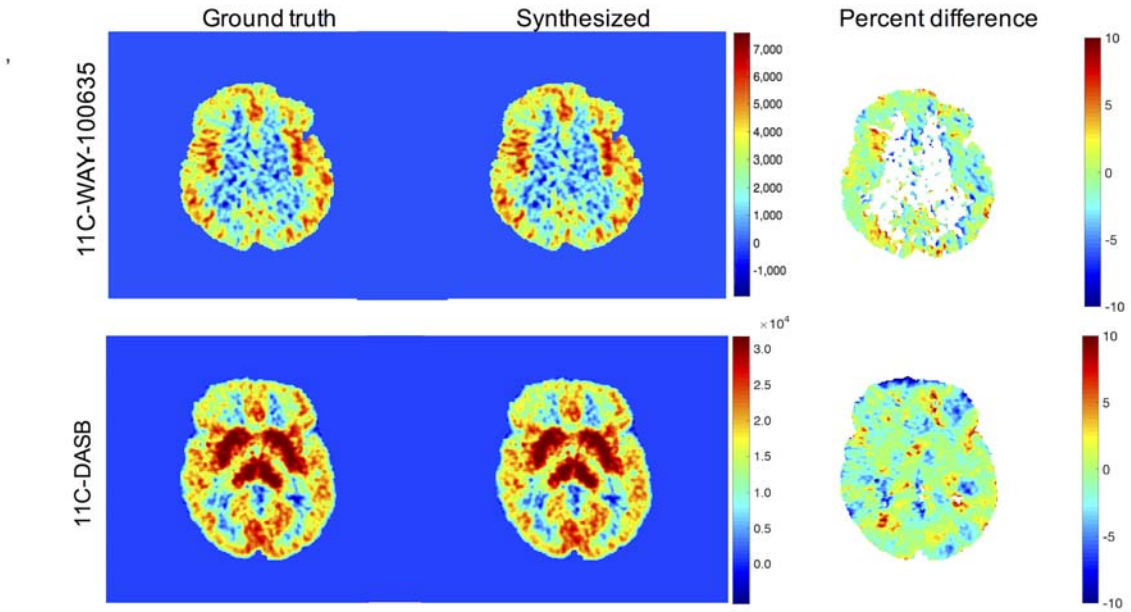


FIGURE 3. PET data reconstructed with ground truth (left) and synthesized (middle) attenuation correction data alongside percent error (right). White voxels in the percent difference images had less than 20% of maximum activity in the ground truth reconstruction and were not included in any reported biases.

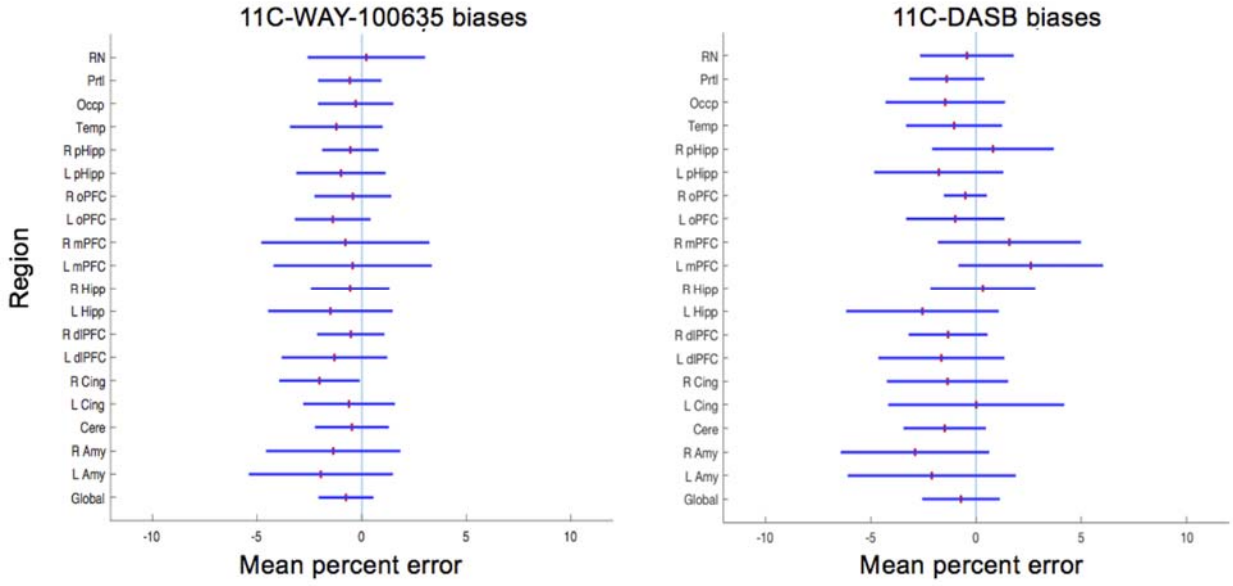


FIGURE 4. Mean bias for all reported ROIs. Red line indicates mean bias, blue horizontal line represents one standard deviation. ROI abbreviations: L/R: Left/Right; RN: Raphe Nuclei; Prtl: Parietal Lobe; Occp: Occipital Lobe; Temp: Temporal Lobe; pHipp: Parahippocampal Gyrus; oPFC: Orbital Prefontal Cortex; mPFC: Medial Prefrontal Cortex; Hipp: Hippocampus; dlPFC: Dorsolateral Prefrontal Cortex; Cing: Cingulate; Cere: Cerebellum; Amy: Amygdala

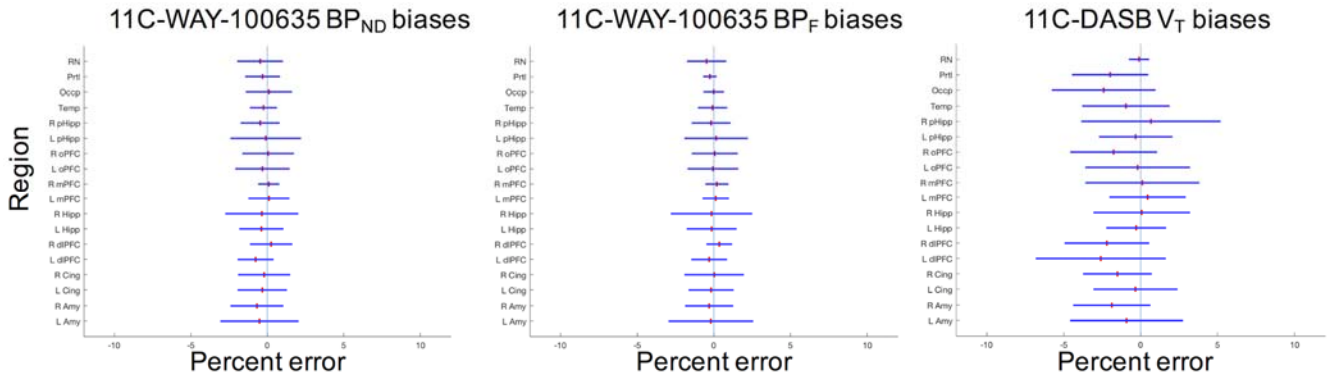


FIGURE 5. Biases for 11C-WAY-100635 $BP_{ND}$ (left) and $BP_F$ (mid) and 11C-DASB $V_T$ (right). Red line indicates mean bias; blue horizontal line represents one standard deviation.

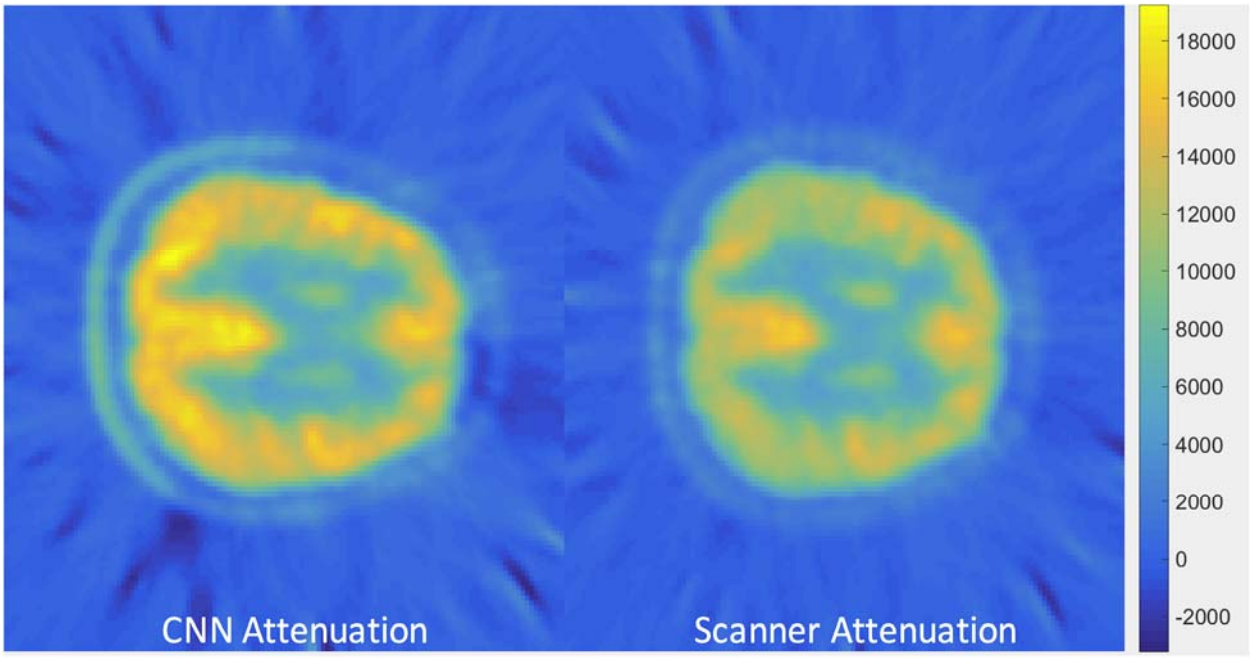


SUPPLEMENTAL FIGURE: 18F-FDG data reconstructed using synthesized (left) and scanner (right) attenuation map provided by Siemens' Biograph mMR. Reconstructed using filtered backprojection.